Accepted to Phys. Fluids 10.1063/5.0139741

Dissimilar Cavitation Dynamics and Damage Patterns Produced by Parallel Fiber Alignment to the Stone Surface in Holmium:Yttrium aluminum garnet Laser Lithotripsy

Gaoming Xiang (项高明)[1], Daiwei Li (李戴薇)[2], Junqin Chen (陈隽沁)[1], Arpit Mishra[1], Georgy Sankin[1], Xuning Zhao (赵旭宁)[3], Yuqi Tang (唐宇琦)[2], Kevin Wang (王冠元)[3], Junjie Yao (姚俊杰)[2], and Pei Zhong (钟培)[1,*]

[1] Thomas Lord Dept. of Mechanical and Materials Science, Duke University, Durham, North Carolina, 27708, USA

[2] Dept. of Biomedical Engineering, Duke University, Durham, North Carolina, 27708, USA

[3] Dept. of Aerospace and Ocean Engineering, Virginia Polytechnic Institute and State University, Blacksburg, Virginia, 24061, USA

[*] Corresponding author: pzhong@duke.edu

Accepted to Phys. Fluids 10.1063/5.0139741

ABSTRACT

Recent studies indicate that cavitation may play a vital role in laser lithotripsy (LL). However, the underlying bubble dynamics and associated damage mechanisms are largely unknown. In this study, we uses ultra-high-speed shadowgraph imaging, hydrophone measurements, three-dimensional passive cavitation mapping (3D-PCM), and phantom test to investigate the transident dynamics of vapor bubbles induced by a Holmium:Yttrium aluminum garnet (Ho:YAG) laser and their correlation with solid damage. We vary the standoff distance (*SD*) between the fiber tip and solid boundary under parallel fiber alignment and observe several distinctive features in bubble dynamics. First, long pulse laser irradiation and solid boundary interaction create an elongated "pear-shaped" bubble that collapses asymmetrically and forms multiple jets in sequence. Second, unlike nanosecond laser-induced cavitation bubbles, jet impact on solid boundary generates negligible pressure transients and causes no direct damage. A non-circular toroidal bubble forms, particularly following the primary and secondary bubble collapses at *SD* = 1.0 and 3.0 mm, respectively. We observe three intensified bubble collapses with strong shock wave emissions: the intensified bubble collapse by shock wave, the ensuing reflected shock wave from the solid boundary, and self-intensified collapse of an inverted "triangle-shaped" or "horseshoe-shaped" bubble. Third, high-speed shadowgraph imaging and 3D-PCM confirm that the shock origins from the distinctive bubble collapse form either two discrete spots or a "smiling-face" shape. The spatial collapse pattern is consistent with the similar BegoStone surface damage, suggesting that the shockwave emissions during the intensified asymmetric collapse of the "pear-shaped" bubble are decisive for the solid damage.

Accepted to Phys. Fluids 10.1063/5.0139741

I. INTRODUCION

In the past two decades, Holmium: YAG (Ho: YAG) laser lithotripsy (LL) with a long pulse duration (≥ 100 μs) has been the treatment of choice for kidney stone diseases [1-5]. The rapid evaporation of fluid near the fiber tip results in an elongated vapor bubble channel (i.e., the Moses effect), which has been primarily believed to facilitate energy delivery and thermal ablation of the stone material during LL, with minimal effect on cavitation damage [6-9]. However, it was discovered recently that cavitation might also play a substantial role in stone fragmentation in LL under high pulse energy ($E_p \geq 0.8$ J) and low frequency ($Freq \leq 10$ Hz) [1], although the dynamics of the vapor bubble and its contribution to stone damage have not been thoroughly investigated.

Extensive studies have been carried out to examine the bubble dynamics and cavitation damage induced by nanosecond (ns) pulsed lasers in water near solid boundaries [10-17]. Both the initial rapid expansion of the bubble and its subsequent violent collapse were found to generate strong pressure transients (i.e., shock waves) and high-velocity liquid jet (up to 100 m/s, [10-12, 18]), impinging upon the solid boundary [12, 15, 16, 19]. However, the damage mechanism remains ambiguous due to small spatiotemporal scales (~hundred micrometers in space and ~microseconds in time) [12, 15, 19]. It is generally observed that the pressure transients emitted from bubble collapse and the resultant damage patterns depend strongly on the bubble's proximity to the boundary, determined by $\gamma = \frac{SD}{R_{max}}$, where SD is the standoff distance between the bubble center and solid boundary, and R_{max} is the bubble radius at maximum expansion in the free field [13-15]. Gonzalez-Avila *et al.* [16] have shown that the ratio of pressure transients corresponding to the primary and secondary collapses also depends on γ. In particular, the pressure transients after the primary bubble collapse are minimum at $\gamma \sim 0.90$ but increase substantially with either smaller or larger γ values [13, 14]. For $1.75 < \gamma < 2.5$, the pressure transients during the secondary collapse are stronger than those produced by the primary collapse of the bubble [16].

In terms of cavitation damage, previous studies have proposed two mechanisms, including the impact of the liquid-jet [17, 18, 20, 21] and the collapse of microscopic bubbles [12, 15], which will result in either single spot damage or ring damage depending on γ. Philipp and Lauterborn [12] demonstrated that the jet impact only contributed to the surface damage at $\gamma < 0.7$, while the circular ring damage pattern was produced during the collapse of a toroidal bubble for $1 < \gamma < 1.7$. Dular *et al*. [22] found that the cavitation damage on thin Aluminum films is more pronounced due to the impact of micro-jet for $\gamma < 0.2$, and the collapse of the microscopic bubbles from the rebound toroidal bubble is more important to the damage produced at $\gamma > 0.5$. In contrast, Tomita et al. [15] proposed that the liquid jet is related directly or indirectly to the plastic deformation of the boundary materials. Particularly, they observed circular ring-like damage patterns for $0.08 < \gamma < 0.32$, which were attributed to the collapse of tiny bubbles formed when the surface of a contracting bubble interacts with the radial flow following a liquid-jet impact. Most recently, Reuter *et al.* observed a different damage mechanism under small γ (≤ 0.20), in which multiple shock waves are emitted during the sequential collapse of the toroidal bubble and converge to a single point, intensify the amplitude of the pressure transients, and create confined holes on the metal substrate [19]. In contrast to ns-pulsed laser generated bubbles, limited research has been performed on fiber laser-induced vapor bubbles and their damage potential on solid boundaries [23-26]. Moreover, the contribution and mechanism of the liquid jet and microscopic bubble collapses to the damage of brittle material (i.e., kidney stones [27]) remains unclear.

Using a parallel fiber arrangement that eliminates direct photothermal ablation in LL, we have recently demonstrated the contribution of cavitation to the surface damage produced on brittle BegoStone phantoms with a strong *SD* dependency [1-3]. In particular, a "smiling-face" damage pattern was produced at $SD = 1$ mm, while a distinctly different single spot damage was observed when *SD* increased to 2 mm with varying bubble size and geometry [1]. However, the mechanism of solid damage caused by these cavitation bubbles and their correlation with the varying bubble dynamics have yet been deciphered [1].

Accepted to Phys. Fluids 10.1063/5.0139741

Among the multiple approaches to investigate cavitation bubble dynamics, high-speed photograph has been widely used in laboratory due to its high frame rate (up to 100 million frames per second, [11]) and high spatial resolution. However, because of the opacity of human tissues, such optical method for cavitation detection has limited utility *in vivo*. In contrast, acoustic methods for cavitation detection, including active cavitation mapping (ACM) and passive cavitation mapping (PCM) [28-30], are more suitable for clinical applications due to the deep tissue penetrating capability of ultrasound. While PCM is promising with high spatiotemporal resolution and penetration depth *in vivo* [28, 29], prior studies utilizing a linear-array ultrasonic probe has limited bubble detection range in the 2D imaging plane of the transducer [29, 31]. For assessing cavitation damage potential in clinical LL, it is important to resolve the time, location, and strength of individual bubble collapses in three dimensions (3D). Thus, 3D cavitation mapping is pressingly needed, such as the 3D-PCM with a 2D array ultrasound transducer initiated by our team in [28].

This study aims to investigate the transient dynamics of Ho:YAG fiber laser-induced vapor bubbles through ultra-high-speed shadowgraph imaging, pressure transient measurements, and 3D-PCM. First, the important contribution of bubble collapse to the damage patterns is investigated for different standoff distances (SD = 1.0 and 3.0 mm) between the fiber tip and the solid boundary, where the fiber is placed parallel to the solid surface. Second, the asymmetric bubble collapse characteristics, such as resulting radial and transverse jets, subsequent toroidal bubble formation/collapse, and shock wave emission and intensification process, are explored. Finally, the damage patterns on a phantom surface have been quantified and correlated with the intensified asymmetric collapse of the bubble and the synchronized 3D-PCM results.

Accepted to Phys. Fluids 10.1063/5.0139741

II. MATERIALS AND METHODS

A. Experimental setup.

The experimental setup is shown in Fig. 1. The vapor bubble was generated by a commercial Ho: YAG laser lithotripter (H Solvo 35-watt laser, Dornier MedTech, Munich, Germany) operated at E_p = 0.8 J and *Freq* = 10 Hz with a pulse duration of 106 μs (measured at full width at half maximum). The pulsed laser is delivered with a 365 μm core diameter fiber (Dornier SingleFlex 400, NA = 0.26, Munich, Germany) into a transparent acrylic container (150 × 150 × 300 mm^3) filled with degassed water. The fiber was aligned parallel to a transparent quartz glass (90 × 60 × 30 mm^3, *x-y-z*) along the *x-y* plane using a three-axis stage and the *SD* between the fiber center and the solid boundary was chosen as 1.0 and 3.0 mm for comparison with previous studies [1].

Cavitation damage was evaluated using BegoStone phantoms (22 × 22 × 4 mm, *L* × *W* × *H*), prepared as described in [1], and treated in water by different pulse numbers (*PN*) up to 100. The fiber tip was placed at the center of the BegoStone sample during LL to eliminate the edge effect on bubble dynamics. After the treatment, the resultant damage on the solid surface was examined by optical coherence tomography (OCT, OQ Labscope, Lumedica, Durham, NC) and quantified using in-house scripts written in MATLAB (MathWorks, Natwickm, MA) [1, 2].

Simultaneous high-speed shadowgraph imaging and hydrophone measurement were used to investigate the bubble dynamics produced near a solid boundary. An ultrahigh-speed camera (Kirana-M5, Specialised Imaging) with a macro lens (Zhong Yi Optics) operated at up to 5 million frames per second (fps) was used to provide a minimum image pixel size of 14 μm. For shadowgraph imaging, the illumination was provided by a 10-ns pulsed laser system (SI-LUX-640, Specialised Imaging) (Fig. 1(a)). In addition, another high-speed camera (Phantom v7.3, Vision Research, Wayne, NJ) operated at 40,000 fps with backlighting provided by a diffused LED was used for imaging the entire bubble dynamics while assisting

the precise alignment of the laser fiber. The pressure transients synchronized with high-speed imaging were recorded using a needle hydrophone (HNC-1000, Onda), which was placed 20 mm from the fiber tip.

Furthermore, high-speed shadowgraph imaging was complemented with 3D-PCM to monitor the 3D bubble activities near the solid boundary comprehensively. A 2D semi-spherical ultrasound array with 256 piezoelectric elements, a central frequency of 4 MHz and 60% bandwidth (Imasonic, Voray, France) was aligned parallel to the solid boundary. The geometric focus (f = 40 mm) of the 2D semi-spherical ultrasound array was co-aligned with the focal plane of the high-speed camera placed from either side-view or bottom-view along the y-z or x-y plane (see Fig. 1(b)). The 2D ultrasound array had a central opening for delivering the illumination light. The passive acoustic signals from the bubble collapse were acquired by a programmable ultrasound scanner (Vantage 256, Verasonics) at a sampling rate of 15.625 MHz. The detected pressure transient signals were converted into voltage signals by the ultrasound array and recorded by the ultrasound scanner for image reconstruction. Using the same 2D ultrasound array, 3D B-mode ultrasound imaging was also performed before and after the LL treatment to calibrate the position of the fiber and solid boundary relative to the array. To synchronize the experimental system, a digital time delay generator (BNC 565, Berkeley Nucleonics Corporation, San Rafael) was used to trigger the high-speed camera, the hydrophone and/or the 3D-PCM system using the trigger output signal from the laser lithotripter.

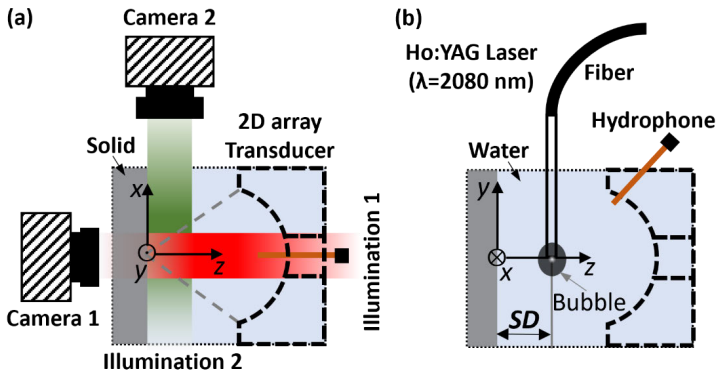

FIG. 1. Schematic representation of the experimental setup for the high-speed shadowgraph imaging, hydrophone measurement, and 3D-PCM. (a) Top view and (b) side view. Standoff distance (*SD*) is defined as the distance between the center of the fiber tip and the solid boundary along the *z*-axis.

B. 3D-PCM reconstruction.

We have previously developed a sliding-window PCM method [29, 31] to determine for the accurate time of the bubble collapse in different locations. In 3D-PCM, the collapsing bubbles can be approximated as sparsely distributed acoustic point sources. We want to determine the correct time origin of the cavitation signal to reconstruct the correct location of the bubble collapse event. To do so, a fixed-size reconstruction window slides along the time axis at each search spot to find the correct time of each bubble collapse. As the sliding-window location is approaching the true bubble collapsing time, the reconstructed bubble image is converging to an increasingly confined region in space. In other words, the most spatially converged bubble reconstruction image indicates that the correct bubble collapsing time has been reached. For each reconstructed instance with different sliding window location, the reconstructed bubble-collapsing strength can be calculated as [30]

$$P_c(\vec{r_s}, t) = \sum_{n=1}^{256} \frac{a(\vec{r_n}-\vec{r_s})}{|\vec{r_n}-\vec{r_s}|} * p_n\left(t + \frac{|\vec{r_n}-\vec{r_s}|}{c}\right), \quad (1)$$

where $P_c(\vec{r_s}, t)$ is the reconstructed bubble-collapsing strength at location $\vec{r_s}$ inside the imaging plane, which is proportional to the reconstructed bubble-collapsing acoustic pressure; a denotes the ultrasound probe's angular detection sensitivity determined by the transducer element's size and frequency; n is the index of the ultrasound probe element (256 elements in total); $\vec{r_n}$ is the location of the nth probe element; p_n is the acoustic signal recorded by the n^{th} element, t is the starting time of sliding window location on the time axis, i.e., delay from the starting time of data acquisition; c is the speed of sound of liquid water that depends on the temperature [32]. The spatial resolution of 2D array around the focus is approximately 0.43

mm, 0.44 mm, and 0.19 mm in *x*, *y*, and *z* directions, respectively. The effective densely sampled 3D field of view of the 2D array transducer is about 10 mm in diameter centered at the focal point of the array.

C. Numerical simulation of the collapse of long pulse laser induced bubble.

3D compressible two-phase flow simulations were performed to predict the evolution of the fluid pressure and velocity fields during the bubble collapse process. Following the methodology described in [33, 34], the 3D Euler equations are solved using a high-resolution shock-capturing finite volume method. The computational domain includes both the bubble and the surrounding liquid water. The thermodynamics of the gas inside the bubble and liquid water are modeled using the perfect gas and stiffened gas equations of state, respectively. The gas-liquid interface, i.e., the bubble surface, is captured implicitly by solving the level set equation. Across the material interface, the mass, momentum, and energy fluxes are computed by constructing and solving exact, one-dimensional Riemann problems, a method known as FIVER (FInite Volume method with Exact two-phase Riemann solvers). The predictive capability of this method has been assessed by simulating laboratory experiments of inertial and shock-induced bubble collapses. It has been shown that the method is able to capture the evolution of bubble geometry and volume, as well as pressure time-histories measured at sensor locations [33, 35].

In this work, the laser fiber and the solid boundary are both modeled as rigidly fixed slip wall boundaries of the fluid domain. The simulation is designed to start at the time when the laser-induced cavitation bubble reaches its maximum size. The size of the initial bubble is determined using high-speed imaging result obtained from the experiment. The velocity of the gas inside the bubble is initialized to be 0. The pressure and density of the gas are set to be close to 0, that is, 400 Pa and 0.957 g/m^3, respectively. The velocity, pressure, and density of the liquid water outside the bubble are set to 0 m/s, 0.1 MPa, and 1000 kg/m^3, respectively. The Euler equations are discretized in space using an unstructured tetrahedron mesh, with minimum element size around 0.04 mm. The simulations are performed on the Tinkercliffs computer cluster using 126 CPU cores. The predicted bubble dynamics (i.e., the 0 level set of the level set function), and the pressure and velocity fields are output and visualized.

Accepted to Phys. Fluids 10.1063/5.0139741

III. RESULTS

A. Distinct cavitation damage features on BegoStone surfaces.

The contribution of cavitation damage to the BegoStone phantom surface is unambiguously established under the parallel fiber arrangement, with the damage morphology, size and spatial distribution all varying distinctly with *SD* and pulse number (*PN*) (Fig. 2(a)). At *SD* = 3.0 mm ($\gamma = 1.07$), two craters (C_A and C_B) are produced along the fiber axis on the BegoStone surface, with C_A, located approximately 1.5 mm below the fiber tip, appearing after 50 pulses and continuing to grow in crater volume up to 100 pulses. In addition, C_B is occasionally observed at about 0.8 mm above the fiber tip and is shallower and smaller than C_A.

At *SD* = 1.0 mm ($\gamma = 0.36$), a drastically different damage pattern is produced on the BegoStone surface, exhibiting an inverted "smiling-face" shape after 100 pulses. The "smiling-face" damage pattern consists of a crater (C_A) located 2.1 mm below the tip and an arc-shaped crater (C_B) above the fiber tip, together with two side craters (left: C_C, right: C_D). The craters, C_A, C_C, and C_D first appear with comparable sizes approximately after 20 pulses. As the *PN* increases, C_C and C_D grow significantly larger in size than C_A, while multiple individual small craters emerge after *PN* = 50 above the fiber tip, eventually forming the arc-shaped crater that connects C_C with C_D. After 100 pulses, the total crater volume produced at *SD* = 1.0 mm ($\gamma = 0.36$) with C_C and C_D contributing about 81%, is 10-fold of the value at *SD* = 3.0 mm ($\gamma = 1.07$), mainly caused by the significant differences in the crater profile area and depth (Fig. 2(b)-2(d)). Overall, the initiation and progression of different damage craters imply a redistribution of the cavitation energy that leads to the initiation and growth of different craters during LL. Such observations motivate us to investigate the detailed bubble dynamics and their correlation with the observed damage patterns produced on the BegoStone surfaces.

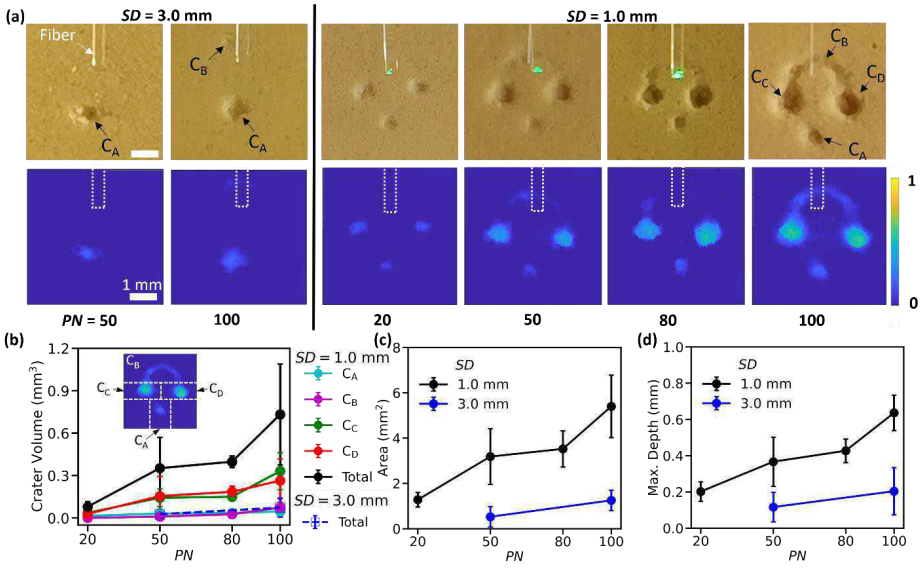

FIG. 2. Distinctly different damage patterns produced on BegoStone phantom surfaces in water at different standoff distances (*SD*) and pulse numbers (*PN*). (a) Top row: photographs, bottom row: OCT reconstruction images of the surface damage. The white dashed lines in the OCT images indicate the fiber. (b) The variation of the total crater volume at *SD* = 3.0 and 1.0 mm, and the volume of the four crater components (C_A to C_D) of the inverted "smiling-face" damage vs. *PN* at *SD* = 1.0 mm ($\gamma = 0.36$). (c) The variation of the crater profile area and (d) maximum depth vs. *PN* at *SD* = 3.0 ($\gamma = 1.07$) and 1.0 mm.

B. Characteristics of cavitation bubble dynamics and associated pressure transients.

In bulk fluid, the Ho: YAG laser-induced vapor bubble grows and collapses axisymmetrically along the fiber axis (Fig. 3(a)). At ~10 μs, an elongated "pear-shaped" bubble is observed, which continues to grow during laser irradiation and reaches a maximum volume at ~330 μs after the cessation of the laser pulse. The bubble volume above the fiber tip resembles a hemispherical shape (see the red half circle in Fig. 3(b)) with the height $H_{1,\,max}$ comparable to the lateral radius $R_{L,\,max}$ ($H_{1,\,max}/R_{L,\,max} = 0.98$), despite the drag

effect of the fiber on bubble expansion. In contrast, due to continued laser evaporation of the liquid at the apex of the bubble [23], the bubble volume below the fiber tip exhibits a cone shape, with the maximum ratio of $H_{2,\ max}/R_{L,\ max}$ reaching 1.31 at 330 μs. Combined, the dimensionless elongation factor η ($= \frac{H_1+H_2}{W_{1,max}+W_{2,max}}$) of the bubble increases from an initial value of 0.98 at 10 μs to a maximum of 1.17 at 110 μs, before decreasing to a minimum of 0.67 at 640 μs during the primary collapse.

The asymmetric geometry of the "pear-shaped" bubble has a profound effect on its collapse dynamics. With a relatively small radius of curvature and thus a strong surface tension effect, the apex of the "pear-shaped" bubble shrinks faster than the upper hemispherical counterpart, forming "Jet 1" (during 330 – 550 μs in Fig. 3a), moving toward the fiber tip. Later, the hemispherical surface of the bubble involutes, forming "Jet 2" (during 610 - 640 μs in Fig. 3(a)) along the fiber axis toward "Jet 1". Shock waves are produced when the bubble collapses to a minimum volume around 640 μs. Thereafter, the bubble rebounds with the distal wall moving away from the fiber tip at a speed of 7.86 m/s (from 700 to 830 μs). These observed features are analogous to the in-phase collapse of tandem bubbles with different sizes in close proximity [36, 37].

The presence of a solid boundary in parallel with the fiber does not substantially alter the elongation factor of the bubble at maximum expansion, with η_{max} rising slightly from 1.14 in the bulk fluid to 1.15 and 1.16 at SD = 3.0 and 1.0 mm, respectively. However, adding a solid boundary will significantly increase the morphological asymmetry of the bubble in the direction transverse to the fiber and normal to the solid surface. Because the expansion of the bubble proximal to the solid boundary (or left from the fiber) is stalled by the boundary, the bubble volume distal to the boundary (or right from the fiber) will increase more rapidly, presumably for maintaining the same total bubble volume produced under the same E_p (Fig. 3(c)). This feature is exemplified by the more dramatic growth in the ratio of the lateral width of the bubble at maximum expansion ($\frac{W_{2,max}}{W_{1,max}}$) with SD from 1.0 in bulk fluid to 1.11 and 2.28 at SD = 3 and 1 mm, respectively. In contrast, the asymmetry of the bubble along the fiber direction, measured by $\frac{H_{2,max}}{H_{1,max}}$, remains

relatively unchanged (1.35 in bulk fluid and ~1.40 at *SD* = 3 and 1 mm). Overall, while the bubble geometry proximal to the boundary varies significantly with *SD*, the bubble geometry distal to the boundary that can expand freely in the fluid remains unchanged, with the ratio of height and lateral width ($\frac{H_{2,max}}{W_{2,max}}$) growth with *SD* exhibiting a similar rate (~1.33).

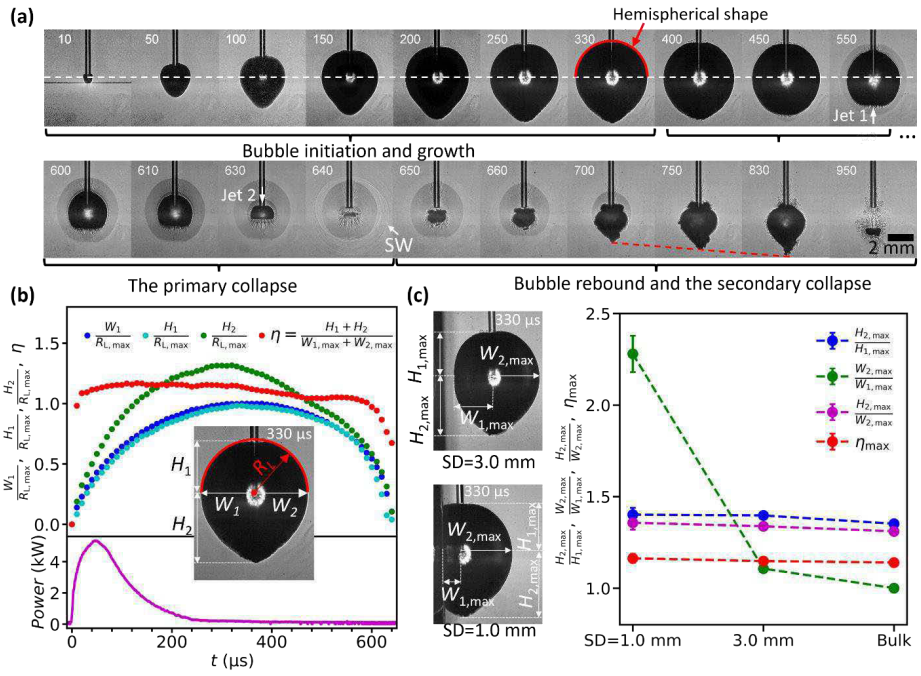

FIG. 3. The dynamics of Ho: YAG laser-induced vapor bubble in bulk fluid and near a solid boundary. (a) Bubble initiation and growth, primary collapse, rebound and secondary collapse in the bulk fluid. The white dashed line indicates the position of the fiber tip. The red dashed line indicates the position of the distal bubble wall during the rebound. (b) Time evolution of normalized geometrical dimensions ($\frac{W_1}{R_{L,max}}$, $\frac{H_1}{R_{L,max}}$, $\frac{H_2}{R_{L,max}}$, and $\eta = \frac{H_1+H_2}{W_{1,max}+W_{2,max}}$) of the bubble and the laser pulse profile (pulse duration = 106 μs, measured at the full width at half maximum). W_1 and W_2 are the lateral width of the bubble at the left

and right of the fiber. Note that $W_1 = W_2 = R_L$ (R_L is the lateral radius) for the bubble in the bulk fluid. H_1 and H_2 are the height of the bubble above and below the fiber tip, respectively, and η is the dimensionless elongation factor of the "pear-shaped" bubble. (c) Comparison of the bubble geometry at its maximum volume near a solid boundary and in the bulk fluid. In (a), "SW" denotes the shock wave. In (b) and (c), the subscript "max" indicates the bubble at its maximum expansion.

Multiple factors, including the secondary Bjerknes forces, surface tension exerted by unsynchronized collapse owing to curvature changes, and a non-uniform flow field, can alter bubble dynamics near a solid boundary [10, 16, 38]. Combined, these effects play an important role during the primary collapse of the bubble at SD = 3.0 mm ($\gamma = 1.07$). Specifically, "Jet 1" starts at the bubble tip with a small radius of curvature and gradually inclines towards the solid boundary (between 330 to 670 μs in Fig. 4(a)), similar to the bubble collapse at a corner [39]. Meanwhile, "Jet 2" from the bubble collapse above the fiber tip is notably different from the case in the bulk fluid: 1) The solid boundary greatly slows down the collapse of the bubble at fiber left, 2) right, the downward liquid flow following the contraction of the bubble is slanted toward the solid boundary, inducing an oblique "Jet 2" at 670 μs in Fig. 4(a).

Unlike the bubble collapse in the bulk fluid, "Jet 2" will not collide directly with "Jet 1" along the fiber direction. Instead, the bubble detaches from the fiber at 690 μs, and the secondary Bjerknes force dominates the later stage of the primary collapse, overtaking "Jet 1" and "Jet 2" and converging them to form a transverse "Jet 3" which advances toward the solid boundary at a speed of 46 m/s (estimated from the right bubble wall positions from 670~700 μs). The trailing fluid of "Jet 3" from the superheated residues of the fluid produced during laser irradiation are apparent as hot filaments in the shadowgraphs [24].

Furthermore, the delayed formation of "Jet 3" after "Jet 1" and "Jet 2" led to a prolonged bubble collapse time when compared to the bubble collapse in the bulk fluid. The transverse jet indicated by the trailing plume of hot liquid pierces the distal bubble wall at 716 μs with negligible pressure transients,

followed by the formation of a toroidal bubble, as demonstrated more clearly in Fig. 4(b) from a repeated experiment captured at 5 Mfps from side-view with simultaneous hydrophone recording. The toroidal bubble disintegrates from 716 to 723 μs, as the instabilities emerge, perhaps triggered by the shear flow that accompanies the "Jet 3" [12, 40], and the bubble energy is released through multiple shock wave emissions along the bubble torus. Thereafter, a cloud of tiny bubbles approaches the solid boundary, with the bulk accumulating below the jet core ("JC", see the white dashed arrow in Fig. 4(b)), where vapor or gas is prevalent.

As shown more clearly from the bottom view in Fig. 4(c-d) from another repeats of the experiment, the collapse of the toroidal bubble is not in unison, but self-intensified. Similar features were observed recently for ns-laser induced bubble collapse [19] . At SD = 3 mm, the toroidal bubble exhibits the shape of an inverted triangle, which collapses initially from the middle of the upper branch of the toroidal bubble right underneath the fiber tip, generating weak shock waves (#1-2). These initial weak shock waves intensify the collapse of neighboring bubbles, exemplified by the two strongly boosted collapses at the two ends of the upper branch of the toroidal bubble (#3-4), with a pressure amplification ratio of 3.5 and a peak pressure of 2.6 MPa. Similar self-intensified collapses from the upper branch of the toroidal bubble (with the projected center of the shockwave emission marked by "*") are also observed from the side-view, with an associated pressure amplification ratio of 3.7 and a peak pressure of 1.39 MPa (see 716 – 718 μs in Fig. 4(b)). Subsequently, the self-intensified collapses progress along the two side branches of the toroidal bubble, leading to a final boosted collapse near the apex of the inverted triangle (#5) where the cloud of tiny bubbles has been accumulated. In addition to the direct incident shock waves, the reflected shock wave (RSW, see 719.6 μs in Fig. 4(b)) from the solid boundary can be observed to interact with the bubble remnants, boosting the final bubble collapse (the center is marked by "+"), doubling the pressure peaks from 720.8 to 722.4 μs. As the bubble remnants continue to translate toward the solid boundary, the shock wave (with the projected center marked by "+") emitted at the apex of the bubble is much closer to the solid boundary than the initial shock waves emitted above the jet core (Fig. 4(b)). Moreover, the Schmidt head

wave (SchW) is observed at 722.8 μs, propagating ahead of the incident and reflected SWs at a characteristic angle of 62.8° from the quartz surface normal (see also the schematic diagram in Fig. 7(b)), indicating the generation of leaky Rayleigh wave (*LRW*) from the shockwave interaction at the fluid-solid boundary [41].

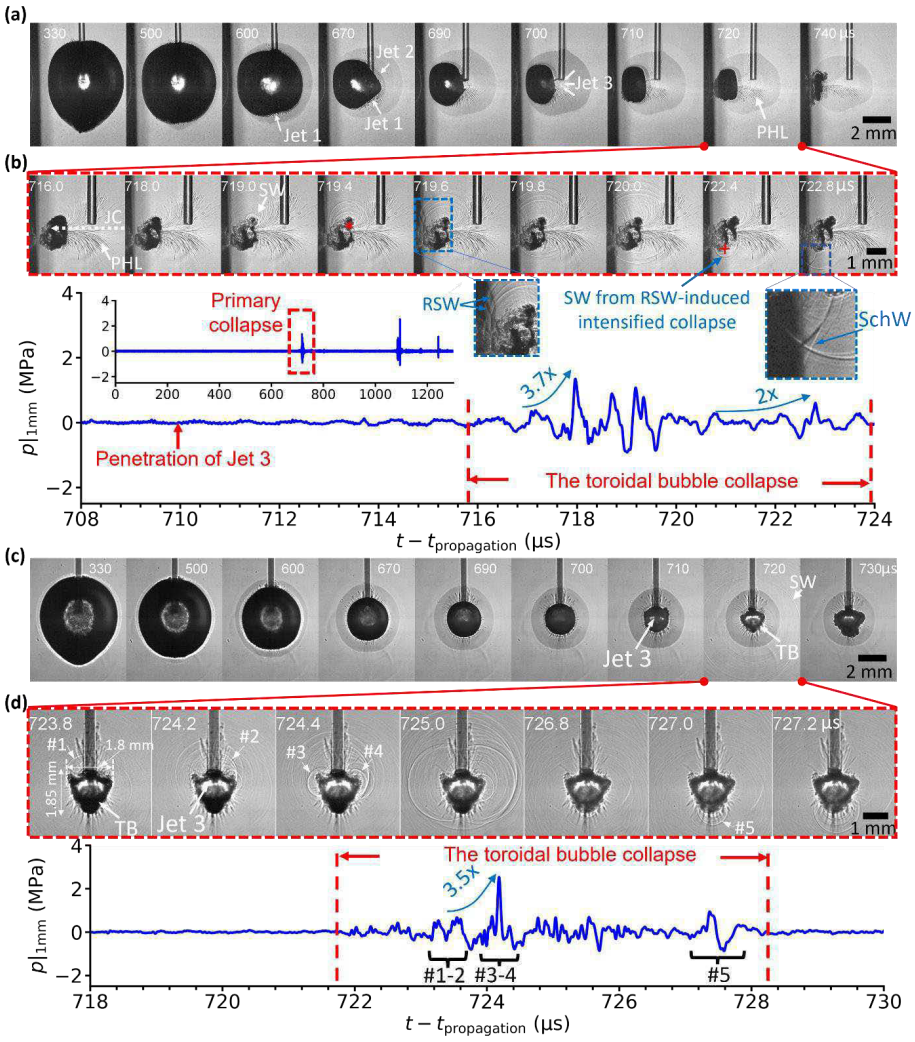

Fig. 4. Dynamics of the primary collapse of the Ho:YAG laser-induced vapor bubble at SD = 3.0 mm (γ = 1.07). Side view high-speed shadowgraph images captured at (a) 100,000 fps, and (b) 5 million fps with simultaneously recorded acoustic pressure transients produced by the primary collapse of the bubble. The blue arrows indicate the boosted pressure emission produced by the self-intensified bubble collapse. The red markers "*" and "+" indicate the projected centers of the self-intensified collapses. $t_{propagation}$ is the estimated propagation time (13.5 μs) of the acoustic wave from the collapsing spot to the hydrophone. Bottome view high-speed shadowgraph images captured at (c) 100,000 fps, and (d) 5 million fps with associated acoustic pressure transients produced by the primary collapse of the bubble. Note that the bubble dynamics in (a-d) were recorded from different bubble events under the same laser setting and SD but different viewing angle and frame rate. Labels #1 to #5 indicate the sequential emissions of the shock waves produced by the self-intensified collapse of the toroidal bubble. Here, "PHL" denotes the plume of hot liquid, "TB" denotes the toroidal bubble, "JC" denotes the jet core, "RSW" denotes the reflected shock wave, and "SchW" denotes the Schmidt head wave [41].

Following the primary collapse, the toroidal bubble rebounds and expands significantly both parallel and normal to the solid boundary (Fig. 5(a)), forming a donut-shaped amorphous structure (Fig. 5(b) and 5(c)). During this process, the trailing "hot" fluid convected by the transverse Jet 3 from the primary collapse is continuously stalled by the solid surface (Fig. 5(b) and 5(c)) and transformed into a splashing radial flow [11]. This transient interaction, coupled with the high pressure built up inside the toroidal bubble during its primary collapse, creates a "sea jelly" like feature at the center while driving concomitantly the expansion of the inner and outer walls of the toroidal bubble during its rebound. After 1015 μs, while the inner wall continues to expand, the outer wall of the donut-shaped toroidal bubble starts to collapse, forming two narrow regions on either sides of the fiber that later pinches off at 1130 μs in Fig. 5(c). Consequently, the pinch-off processes break up the donut-shaped toroidal bubble into two daughter bubbles, a small one above and a large one below the fiber tip at 1135 μs (Fig. 5(c)). The daughter bubble below the fiber tip is

larger as more vapor or non-condensable gas accumulates below the jet core (see Fig. 4(b)). Finally, the two daughter bubbles shrink rapidly from their ends (with small radii of curvature) to the central section in the middle, emiting a weak shock wave of 1.61 MPa at 1139 μs above, and a stronger shock wave of 2.96 MPa at 1150 μs below the fiber tip, respectively (Fig. 5(c)) and close to the solid boundary (Fig. 5(a)).

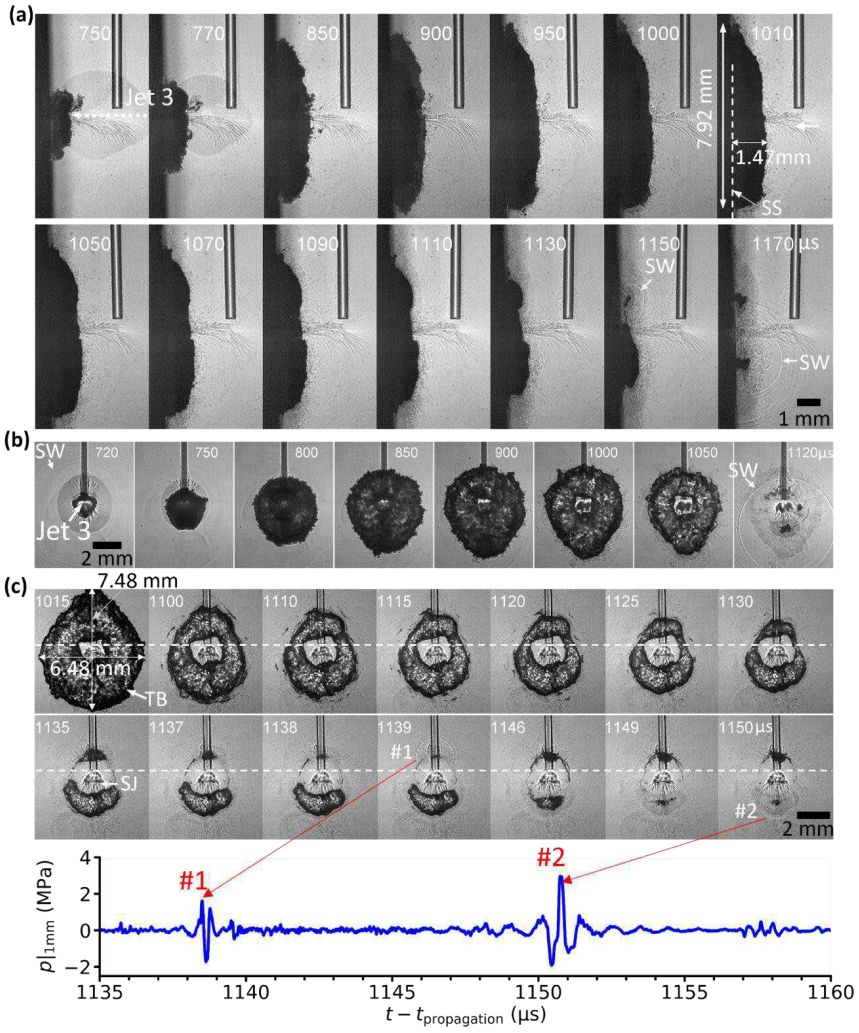

Fig. 5. Representative high-speed shadowgraph images of the rebound and secondary collapse of the toroidal bubble at SD = 3.0 mm ($\gamma = 1.07$). (a) Side view and (b) bottom view captured at 100 kfps, and (c) bottom view captured at 1 Mfps (from another repeat) with associated pressure transients. The white dashed line in (c) indicates the location of the fiber tip. Here, "SS" denotes the solid surface, and "SJ" denotes the sea jelly like feature.

As the fiber moves closer to the solid boundary, i.e., SD = 1.0 mm ($\gamma = 0.36$), while the height is similar the "pear-shaped" bubble expands most significantly on the right side of the fiber, compared to those at SD = 3.0 mm ($\gamma = 1.07$) and in the bulk fluid (see also Fig. 3(c)), creating a bell-shaped maximum bubble [38] expansion on the solid boundary (500 μs in Fig. 6(a)) with a longer collapse time (~780 μs vs. ~ 720 μs for SD = 3 mm). During the primary collapse of the bubble, the process starts similarly with Jet 1 protruding from the bottom at 650 μs and Jet 2 from the upper surface of the bubble at 700 μs along oblique angles from the fiber axis, and subsequently joining Jet 3 from 720 to 750 μs in the direction perpendicular to the solid boundary, as shown in Fig. 6(a). The speed of Jet 3 is about 28 m/s, estimated from the right bubble wall positions between 700 and 750 μs, which is smaller than its counterpart (46 m/s) at SD = 3 mm.

At SD = 1.0 mm ($\gamma = 0.36$), another significant change is that the bubble wall left to the fiber is attached to the solid boundary and contracts at a slower speed of 8.4 m/s (measured from the lateral radius of the bubble from 650 to 750 μs in Fig. 6(b)) in the direction parallel to the solid boundary than its counterpart of 10.4 m/s at SD = 3 mm during the primary collapse. Because of the cushion effect of the abundant vapor/gas accumulated inside the bubble during laser irradiation, the impact of Jet 3 produces negligible pressure transient. The jet speed at touch down is significantly reduced, such that either the resultant water hammer pressure or stagnation pressure has fallen below the hydrophone detection sensitivity range. However, the impact of Jet 3 produces a splashing radial flow on the solid boundary that

drives the formation of a larger toroidal bubble (see 750 ~ 770 μs in Fig. 6(b)). Notably, the upward movement of Jet 1 near the bubble apex counteracts with the radial jet from the splashing flow along the solid surface, creating a flattened region of stagnated flow at the bottom, see 760 – 770 μs in Fig. 6(b), while the upper part of the toroidal bubble remains in a circular shape during the collapse, generating multiple shock waves with features of self-intensified collapse for the toroidal bubble revealed in the pressure trace (see 770 – 780 μs in Fig. 6(b)).

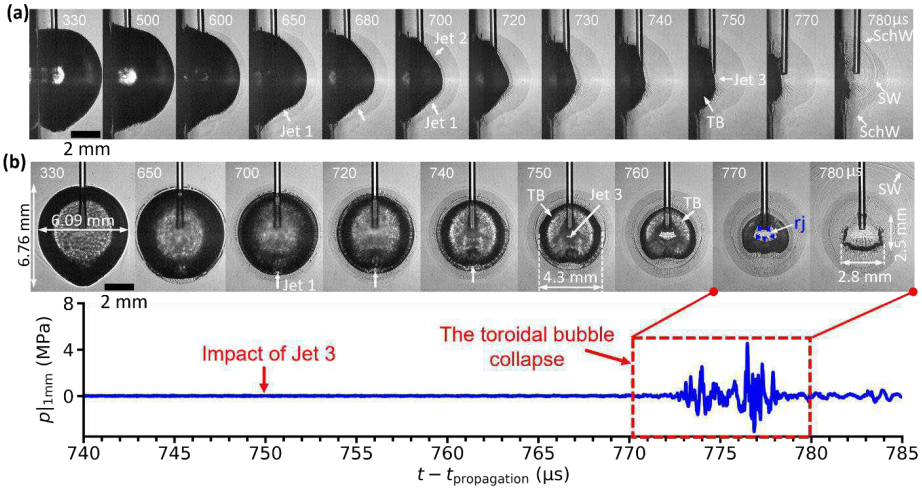

Fig. 6. Dynamics of the primary collapse of the Ho: YAG laser-induced vapor bubble captured at 100,000 fps at SD = 1.0 mm ($\gamma = 0.36$). Shadowgraph images from (a) side-view, (b) bottom view with simultaneously recorded pressure transients. The blue arrows indicate the radial jet ("rj").

The final stage of the toroidal bubble collapse at SD = 1 mm ($\gamma = 0.36$) is captured at 5 million fps with distinct features illustrated schematically in Fig. 7. First, the upper circular branch of the toroidal bubble is attached to the solid boundary on one side and with its middle portion in contact with the fiber tip on the other side. The collapse of the toroidal bubble is driven by the opposite movements of its outer wall

contraction and the radial jet expansion from inside, leading to pinch-off on two sides of the fiber (777 - 778 μs). This breakdown of the toroidal bubble forms a small daughter bubble attached to the fiber tip on the upper part and a large "horseshoe-shaped" bubble in the lower part. The pinch-off regions have small radii of curvature, which initiates the collapse of the small daughter bubble underneath the fiber tip, emitting the 1st series of shock waves with a boosted peak pressure of 2.3 MPa (#1 in Fig. 7(a)). Second, under the influence of these initial shock waves, the "horseshoe-shaped" bubble collapses subsequently at its opening ends on both sides of the fiber, generating the 2nd and 3rd shock waves (#2 - #3) at 779.6 μs. Third, the collapse of the remaining "horseshoe-shaped" bubble spreads along the two side branches toward the two corners at 780.8 μs, followed by the flattened bottom branch contracting into a thin minimal volume. During this process, the "hot" filaments around the "horseshoe-shaped" bubble (i.e., the region indicated by the white dashed line in Fig. 7(a)) is clearly visible, indicating high temperature with abundant vapor or non-condensable compressed gases trapped in those regions [24, 42] that may dampen the bubble shrinkage. At 781.2 μs, the remaining bubble pinches off near the two corner locations, and collapses violently, generating the strongest boosted shock waves (#4 – #5) with the peak pressure reaching up to 7.1 MPa (Fig. 7(c)).

Altogether, the primary collapse of the toroidal bubble bubble at SD = 1.0 and 3.0 mm is exemplified by the non-unison yet self-intensified collapsing processes with similar durations (~8 μs) and pressure amplification ratios (~ 3.5 x). In comparison, however, the centers of the self-intensified collapses are closer to the solid boundary with higher maximum peak pressures at SD = 1.0 mm ($\gamma = 0.36$) than their counterparts at SD = 3.0 mm ($\gamma = 1.07$).

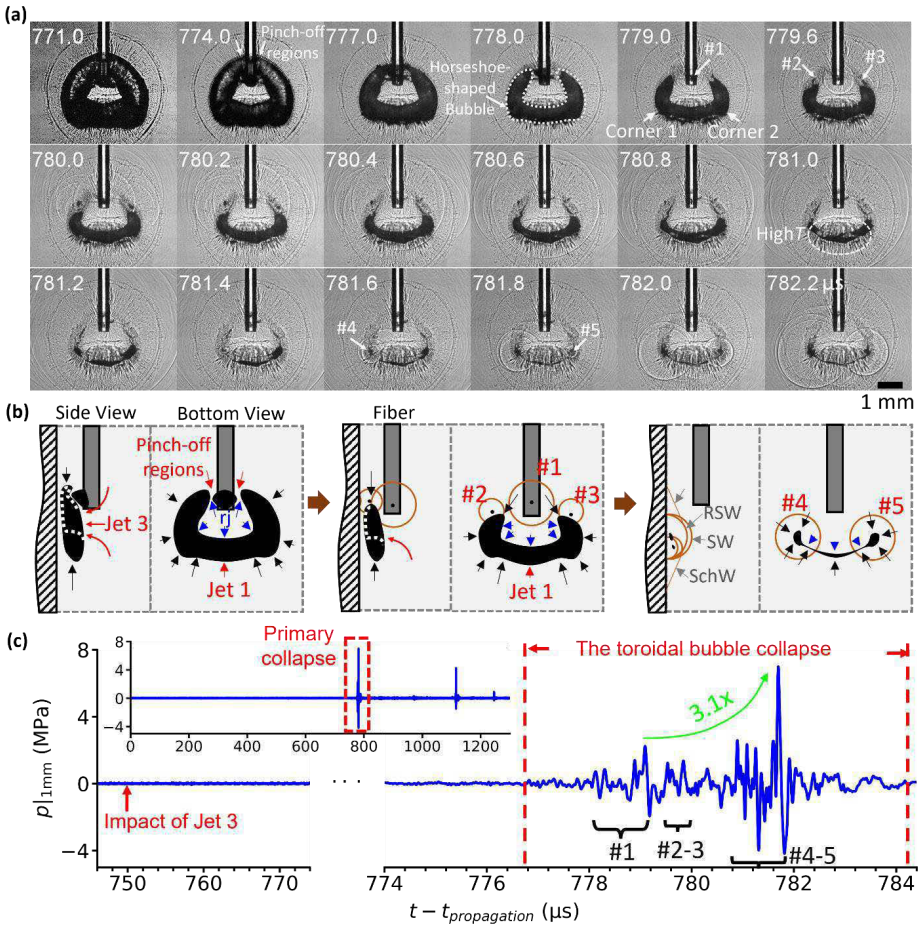

FIG. 7. Detailed dynamics of the toroidal bubble collapse at SD = 1.0 mm (γ = 0.36). (a) High-speed shadowgraph images captured at 5 million fps, revealing the pinch-off of the toroidal bubble in the upper part on both sides of the fiber, breaking into a small daughter bubble attached to the fiber tip and a "horseshoe-shaped" large daughter bubble on the lower part. (b) Schematic illustration of the liquid jet impact normal to the solid boundary, and resultant formation and collapse of the toroidal bubble with five distinct locations where the shock wave emissions are observed. (c) The associated pressure transients

produced during the final stage of the primary collapse of the toroidal bubble in (a). Labels #1 to #5 indicate the self-intensified shock wave emissions generated by the sequential collapse of the toroidal bubble.

Finally, because of the strong primary collapse, the rebound of the toroidal bubble at SD = 1.0 mm ($\gamma = 0.36$) (Fig. 8) is much weaker with smaller dimensions than its counterpart at SD = 3.0 mm ($\gamma = 1.07$) (see Fig. 5). The small and large daughter bubbles rebound separately on the solid boundary, with the small bubble collapsing sooner and weakly above the fiber tip at about 980 μs (#1 in Fig. 8(b)). In contrast, after the first rebound the large "horseshoe-shaped" bubble grows into a mask-shape (at 900 – 970 μs in Fig. 8(b)) and eventually transforms into a hemi-spherical bubble on the solid surface, collapsing strongly to a spot located 1.75 mm below the fiber tip (#2 in Fig. 8(b)). During this secondary collapse, the bubble wall parallel to the solid boundary contracts with the average velocities $\left|\boldsymbol{v}_y^+ - \boldsymbol{v}_y^-\right| = 30.3$ m/s (measured from 1050 to 1110 μs in the side view) and $|\boldsymbol{v}_x^+ - \boldsymbol{v}_x^-| = 35.5$ m/s (measured from 1050 to 1100 μs in the bottom view) higher than the bubble wall collapsing velocity toward the solid boundary ($|\boldsymbol{v}_z| = 9.8$ m/s, measured from 1050 to 1110 μs in the side view). As a result of such a rapid circumferential contraction, strong shock waves with a peak pressure of 3.9 MPa are generated by the secondary collapse at about 1110 μs and likely very close to the solid boundary (at 1120 μs in Fig. 8(a)).

Accepted to Phys. Fluids 10.1063/5.0139741

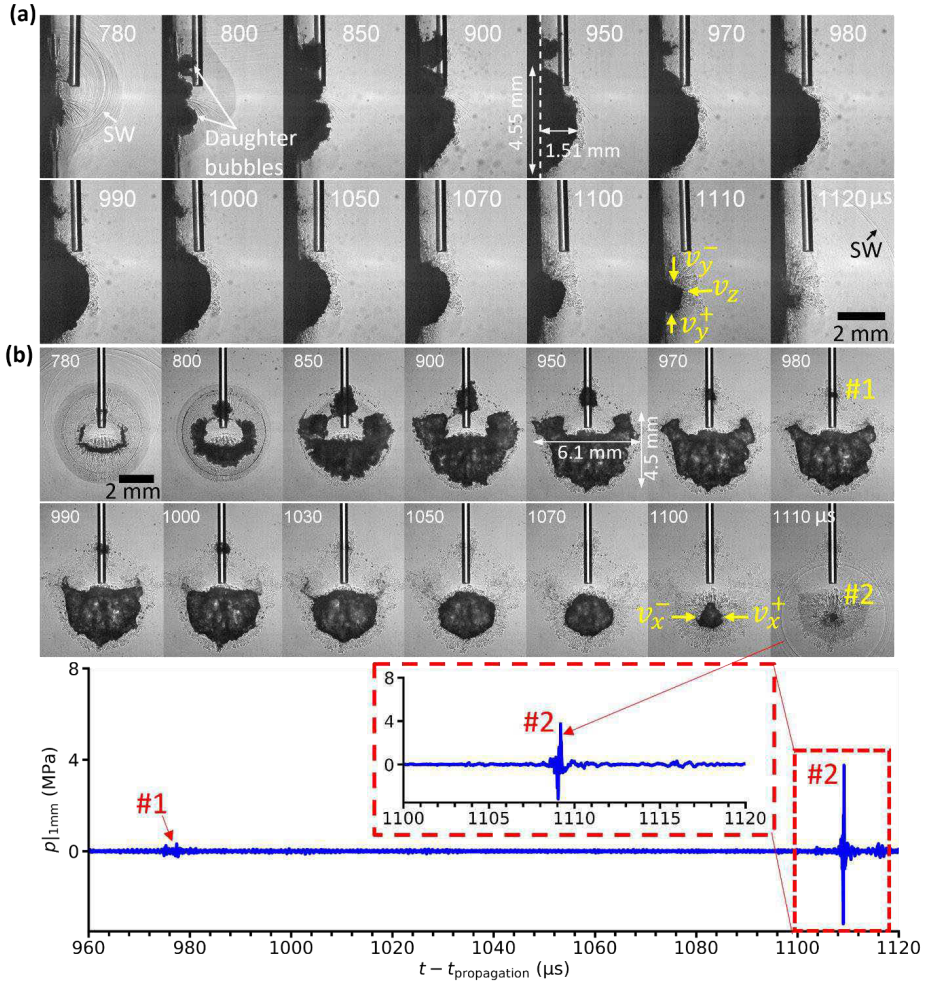

Fig. 8. The dynamics of the rebound and secondary collapse of the Ho:YAG laser induced vapor bubble at *SD* = 1.0 mm. Selected high-speed shadowgraph images captured at 100 kfps (a) in side view and (b) bottom view along with associated pressure transients produced during the secondary collapse of the bubble.

C. Correlation between bubble collapse and resultant damage on BegoStone surface.

In the following section, the cavitation bubble collapse detected by 3D-PCM is compared with the simultaneous high-speed shadowgraph images of the same bubble event. In addition, the pattern of the damage craters produced on the BegoStone surfaces is correlated with the characteristics of the shock wave emission sequence, locations and strengths from the primary and secondary collapses of the bubble near a glass surface.

1. Synchronized high-speed shadowgraph imaging and 3D-PCM.

For validation, the locations of the collapsing spots from 3D-PCM are directly compared with shock origins extracted from high-speed shadowgraph images taken from two projection angles under SD = 1.0 mm ($\gamma = 0.36$) (Fig. 9). The sequential collapse of the toroidal bubble from near the fiber tip (785 μs) to the two corners of the "horseshoe-shaped" bubble (786.4 μs) observed in the high-speed images is well captured by the 3D-PCM results (Fig. 9(a)). The location deviations of the collapsing spots between the 3D-PCM and high-speed images are less than 0.16, 0.23 and 0.02 mm in x, y, and z directions, respectively (see a comparison summary of the x-y-z coordinates in Table S1). The bubble-collapsing strength P_C (defined in eq. (1)) at the two corners of the horseshoe-shaped bubble is stronger than those along the bubble torus. Furthermore, the secondary collapse of the toroidal bubble after rebound to a single spot below the fiber tip and near the solid boundary is also resolved by the 3D-PCM (see Fig. 9(b)). Overall, these results demonstrate that 3D-PCM can faithfully map the bubble collapsing locations and strength in 3D space within the spatial resolutions of the 2D array system ($0.43 \times 0.44 \times 0.19$ mm in x-y-z directions) [28].

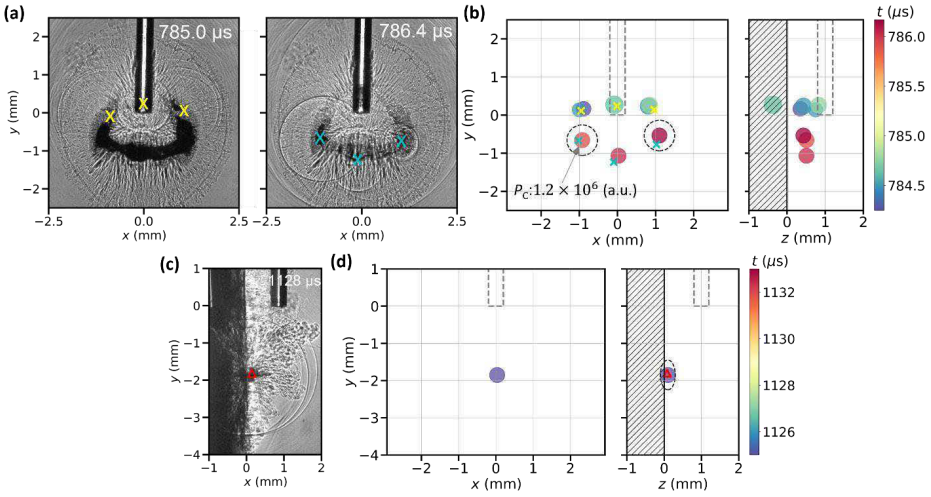

FIG. 9. Representative high-speed shadowgraph images (a, c) of the Ho:YAG laser-generated bubble collapse and associated shock wave emission in comparison with the reconstruction results of simultaneously acquired 3D-PCM in terms of collapsing location, time, and strength (b, d). (a) Primary bubble collapse from the bottom view, (b) the associated collapsing spots from PCM reconstruction results in the *x*-*y* and *z*-*y* planes, (c) secondary bubble collapse from the side view, and (d) the associated collapsing spots from PCM reconstruction results in the *x*-*y* and *z*-*y* planes. The two dashed circles indicate the possible locations of two representative collapsing spots within the resolution of the 3D-PCM. The circle color indicates the collapsing time, and the circle size is scaled with the reconstructed bubble-collapsing strength (P_C, see eq. (1)). Here, markers "x" and red markers "Δ" indicate the shock origins from the primary and secondary collapse, respectively. The fiber was placed at SD = 1.0 mm (γ = 0.36) parallel to the solid boundary, and E_p = 0.8 J.

2. Correlation between the surface damage and shock waves emitted from the bubble collapse.

For the shock waves generated by the bubble collapse, the strength decays rapidly following the $1/r$ law [13]. Therefore, the highest damage potential will be produced at the bubble collapsing sites close to the solid boundary. Figure 10 compares the locations of shock origins within 0.7 mm from the solid boundary captured by high-speed imaging and the crater positions on the BegoStone surface evaluated by OCT (see Fig. 2(a)). At SD = 3.0 mm ($\gamma = 1.07$), the positions of the two craters produced along the fiber axis (C_A and C_B) in are in good agreement with the shock origins from the primary (727.2 μs) and secondary (1150 μs) collapses of the lower part of the toroidal bubble below the fiber tip, and with the secondary collapse of the upper part of the toroidal bubble above the fiber tip (Fig. 10(a)). In contrast, at SD = 1.0 mm, the largest craters produced on both sides of the fiber (i.e., C_C and C_D) match well with the shock waves originated from the primary collapse at the corners of the horseshoe-shaped bubble (782.2 μs) while the arc region above the fiber tip (C_B) matches with the shock origins from the small bubble collapses in the middle and near the two ends of the horseshoe-shaped bubble (779.6 μs in Fig. 10(c)). In addition, a small crater C_A below the fiber tip is produced by the secondary collapse of the toroidal bubble after rebound (1104 μs in Fig. 10(c)).

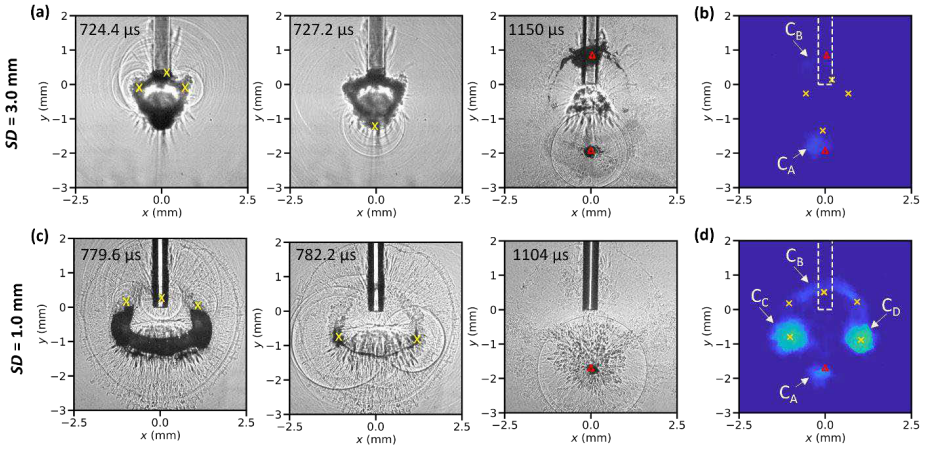

FIG. 10. Correlation between the shock origins from the bubble collapse near a glass surface and the damage craters observed on BegoStone surfaces following LL. Selected shadowgraph images of the

primary and secondary collapse of the bubble near a glass surface with shock wave emission from the bottom view at (a) *SD* = 3.0 mm ($\gamma = 1.07$) and (c) *SD* = 1.0 mm ($\gamma = 0.36$). Representative OCT image of surface damage pattern on BegoStone phantoms after 100 laser pulses at (b) *SD* = 3.0 mm ($\gamma = 1.07$) and (d) *SD* = 1.0 mm ($\gamma = 0.36$). Here, yellow markers "x" and red markers "Δ" indicate the shock origins from the primary and secondary toroidal bubble collapse, respectively. The dashed lines in the OCT images denote the position of the fiber in the *x*-*y* plane.

IV. Discussion

We have conducted comprehensive investigations using high-speed shadowgraph imaging, phantom tests, hydrophone measurements, and 3D-PCM to understand the transient dynamics of elongated vapor bubbles induced by Ho:YAG fiber laser at different *SD*s parallel to a solid boundary. Several novel insights into the physics of vapor bubble dynamics and their correlations with the damage produced on the solid surfaces have been uncovered and are discussed further below.

First, the "pear-shaped" bubble induced by the Ho: YAG fiber laser in the bulk fluid (i.e., water) has prolongated expansion (330 μs for $R_{\mathrm{L,max}} = 2.8\,\mathrm{mm}$) and collapse period (310 μs) compared to the Rayleigh collapse time $T_{\mathrm{C}}^{\mathrm{Rayleigh}}$ (= 256 μs) of a spherical bubble with equivalent radius ($R_{\mathrm{max}} = R_{\mathrm{L,max}}$), given by [43, 44]

$$T_{\mathrm{C}}^{\mathrm{Rayleigh}} = 0.915 R_{\mathrm{max}} \sqrt{\frac{\rho}{(p_{\mathrm{stat}} - p_{\mathrm{v}})}}, \tag{2}$$

where ρ denotes the density of the liquid, p_{stat} is the static pressure, and p_{v} is the vapor pressure of the liquid. The elongation during the bubble expansion (see Fig. 2) is driven by the continued superheating of the fluid at the apex of the bubble due to the long duration of laser irradiation (~210 μs), which will lengthen the expansion to collapse time of the bubble [14]. In addition, the abundant vapor or non-condensable gas produced inside the bubble will dampen its collapse, and thus further prolong the collapse time [42].

Considering that the upper part of the "pear-shaped" bubble approximates a hemisphere (see Fig. 3(a)), the dimensionless standoff distance of the bubble to the solid boundary $\gamma = \frac{SD}{R_{\mathrm{L,max}}}$ is estimated to be 0.36 and 1.07 for *SD* = 1.0 and 3.0 mm, respectively. The formation of a toroidal bubble following the liquid jet impact on the solid boundary is consistent with such feature observed for ns laser-induced bubbles under γ < 1.7 [12].

Furthermore, several general features associated with the fiber laser induced vapor bubble collapse near a solid boundary were captured by numerical simulations. Details of the pressure and velocity fields around the collapsing bubble are depicted in Fig. 11(a) at various time instants. Note that the tip jet ("Jet 1" in Fig. 4(a)) was not captured due to the initially spherical bubble geometry used in the simulation. However, the region of liquid water right above the bubble is found to have higher pressure compared to other regions near the bubble at around 670 μs, leading to the formation of a liquid jet ("Jet 2") at 690 μs with increased pressure and downward velocity. This jet is not perfectly perpendicular to the wall, indicating the influence of the laser fiber. Subsequently, another jet ("Jet 3") forms with higher pressure and velocity at around 710 μs. The bubble collapse time (~ 400 μs) and jet formation toward the wall surface instead of along the fiber axis are in good agreement with the experimental observations (see Fig. 4).

Nevertheless, the model still needs further refinements to fully capture the bubble dynamics in LL. Figure 11(b-c) shows the pressure and velocity fields at 718 μs using a full scale that capture the extreme values at this time. The maximum pressure is around 3 MPa, and the jet velocity is around 150 m/s, which is substantially higher than the transverse jet speed (46 m/s) measured experimentally at *SD* = 3.0 mm (γ = 1.07) (Fig. 4). The discrepancy may be caused by the significant damping effect in LL-induced vapor bubble collapse and the neglection of the lateral contraction effect of "Jet 1" prior to the formation of "Jet 3". In addition, the model simulation stopped when the opposite bubble walls touched each other, and no bubble rebound or secondary collapse could be simulated in comparison with the experimental observations.

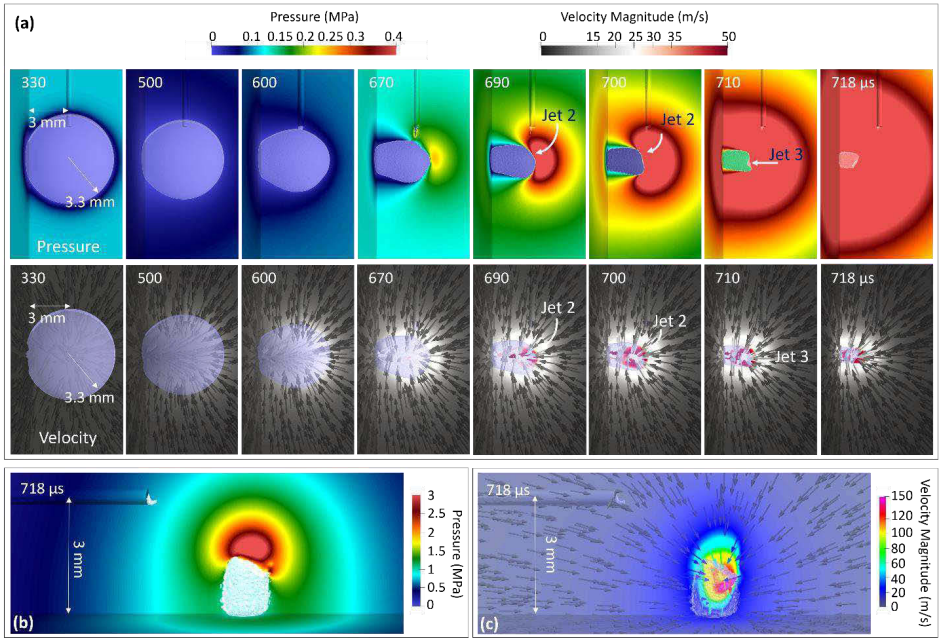

Fig. 11. Numerical simulations of the collapse of a spherical bubble at SD = 3.0 mm (γ = 1.07). (a) Snapshots of the predicted bubble geometry, fluid pressure and velocity field at 8 different time instants. (b) A close-up image showing the predicted pressure field at 718 µs. (c) A close-up image showing the predicted velocity field at 718 µs. The simulation time axis has been synchronized with the experiment (Fig. 4) for ease of comparison. In the velocity images, the magnitude of velocity is shown in color with the direction marked by arrows.

Second, although asymmetric bubble collapse with jet formation toward the solid boundary is a general feature in LL, the jet speed is typically below 50 m/s and no apparent pressure transients are generated by the jet impact on the solid boundary (see Figs. 4, 6-7). Instead, the jetting flow drives the formation of a toroidal bubble near the solid boundary and strong shock waves are generated by the non-unison collapse

of the toroidal bubble with a progressive compression of its gas content, boosted by the self-intensified collapsing process (see Fig. 7). The pressure amplification ratio of the shock wave induced self-intensified collapse of the toroidal bubble can reach up to 3.7 (Fig. 4(b)), which is close to the pressure amplification ratio of 4.8 produced by a lithotripter-generated shock wave interaction with ns pulsed laser-induced inertial bubbles [45].

In comparison to the circular toroidal bubble produced by ns laser-induced bubble collapse under $\gamma \leq 0.2$ [19], the toroidal bubble produced by LL is non-circular, e.g., in horseshoe-shape at SD = 1.0 mm ($\gamma = 0.36$) or inverted triangle-shape at SD = 3.0 mm ($\gamma = 1.07$). The long sub-millisecond laser irradiation, compounded by the multiple interactions of the vapor bubble with the fiber tip and solid boundary, results in an anisotropic expansion of the radial jet (see Fig. 6), leading to the formation of a non-circular toroidal bubble with non-uniform geometry. Consequently, the collapse of the toroidal bubble is initiated by instability at pinch-off spots of small radius of curvature and low vapor content, i.e., above the fiber tip, and propagates along different branches through the self-intensified collapsing process to reach the end of each branch (on either side of the fiber) where the radius of curvature of the toroidal bubble changes abruptly (see Fig. 4(c) and Fig. 7(a)). At these corners, the boosted shock wave emissions will further initiate the collapse of the remaining branches of the toroidal bubble below the fiber tip where the vapor content is high. It is worth noting that while the strongest shock waves are generated at the end of the branches where the vapor content is low, weak shock waves are produced by the collapse of the toroidal bubble branch with high gas/vapor content due to its cushioning effect. In comparison, the shock waves emitted from the collapse of ns-laser induced circular toroidal bubble will progress continuously from one end of the bubble torus to the other, converging the collapsing energy to a single spot to produce damage in a drilled like hole on the material surface [19].

Third, as summarized in Fig. 12, the maximum peak pressure at 1 mm from the collapse site ($p|_{1\text{ mm}}$), the pressure impulse (PI), and the acoustic energy associated with the emitted shock wave (E_s) from the primary, secondary and tertiary collapses of the LL-generated vapor bubble near the solid boundary all vary

dissimilarly with SD (or γ). In close proximity to the solid boundary at SD = 1.0 mm ($\gamma = 0.36$), the primary collapse of the bubble produces the highest peak pressure (5.3 MPa), PI (2.99 Pa·s), and E_s (0.036 mJ), followed by the secondary and tertiary collapses (see Fig. 12(a) to 12(c)). The average ratios in p_1/p_2, PI_1/PI_2, and $E_{s,1}/E_{s,2}$ between the primary and secondary collapses are 1.46, 4.52, and 4.45, respectively, all greater than 1. These results suggest that the initial bubble potential energy is largely released by acoustic emission or dissipated by heat transfer during the primary collapse with less energy retained within the bubble after each rebound [14]. These progressively weakened collapses are similar to the characteristics in ns laser-induced bubble collapses near a solid boundary [13].

In contrast, distant from the solid boundary at SD = 3.0 mm ($\gamma = 1.07$), the secondary collapse of the bubble becomes the strongest with p_1/p_2, PI_1/PI_2, and $E_{s,1}/E_{s,2}$ ratios of 0.67, 0.45, and 0.36, respectively, all less than 1. Specifically, PI_2 and $E_{s,2}$ at SD = 3.0 mm ($\gamma = 1.07$) are about 2.5- and 1.6-fold of the corresponding values at SD = 1.0 mm ($\gamma = 0.36$), respectively. It is worth noting that because the bubble wall is not attached to the boundary surface under this condition, a ring vortex is produced near the final stage of the primary collapse that partially transforms the kinetic energy associated with the jet impact and resultant radial flow into energy of rotation with the bubble content less compressed [14]. The ring vortex also encirculates hot water produced near the bubble apex into the jet core (see Fig. 4(b)), and thus entrapping more vapor and non-condensable gas inside the small inverted triangle-shaped toroidal bubble, especially in the branches below the fiber tip (see 723.8 μs in Fig. 4(d)). As a result, the primary collapse is significantly dampened, the volume compression ratio of the toroidal bubble is estimated to be on the order of 10 (the volume of the toroidal bubble is proportional to the product of the area of the cross section and ring diameter of the toroidal bubble) with relatively large minimal volume (see Fig. 4), leading to weak pressure transients. On the other hand, the intense cushioning effect on the primary collapse also suggests that significant energy is retained inside the compressed gas at the minimal volume of the bubble, leading to a strong rebound to a large-sized toroidal bubble (6.5 × 7.5 mm) and subsequently, a stronger secondary collapse (see Fig. 5(c)). In comparison, at SD = 1.0 mm ($\gamma = 0.36$) the bubble wall is attached to the solid

boundary and jet impact does not produce ring vortex under such condition ($\gamma = 0.36$) [14], leading to less hot water engulfed into the collapsing bubble and possibly lower vapor and non-condensable gas entrapped inside the toroidal bubble during the final stage of the collapse (see Fig. 6). The jet impact and associated radial flow compress directly on the bubble content to drive the resultant toroidal bubble expansion to a large size (see 750 ~ 780 μs in Fig. 6(b)). Consequently, the primary collapse, boosted by a stronger self-intensified collapsing process, is more violent with the estimated volume compression ratio on the order of 10^3 as the toroidal bubble is much smaller at the minimum size, leading to strong shock wave emissions (see Fig. 7). As a result, the rebound is weaker, leading to a small-sized toroidal bubble (6.1 × 4.5 mm) and an associated less intensive secondary collapse (see Fig. 8(b)).

Furthermore, the minimum distance ($d_{c,min}$) of the shock origin from the bubble collapse to the solid boundary determines the maximum energy density ($\propto \frac{E_{s,1}}{(d_{c,min}^{1st})^2}$) delivered to the solid boundary, which may correlate with damage potential. Such minimum distance changes significantly with *SD,* e.g., the value of $d_{c,min}$ from the primary to the secondary collapse of the bubble increases from 0.06 mm to 0.2 mm at *SD* = 1.0 mm ($\gamma = 0.36$); in contrast the corresponding value decreases from 0.5 mm to 0.2 mm at *SD* = 3.0 mm ($\gamma = 1.07$) (Fig. 12(e)). Consequently, the energy density ratio, $\frac{E_{s,1}}{E_{s,2}} \cdot \left(\frac{d_{c,min}^{2nd}}{d_{c,min}^{1st}}\right)^2$, reaches 57 at *SD* = 1.0 mm ($\gamma = 0.36$), which is significantly higher than the corresponding value of 0.04 at *SD* = 3.0 mm ($\gamma = 1.07$) (Fig. 9(f)). These results suggest that the primary collapse of the bubble is the dominant contributor to the damage produced on the BegoStone phantom surfaces at *SD* = 1.0 mm ($\gamma = 0.36$), whereas the secondary collapse may play a more important role in stone damage at *SD* = 3.0 mm ($\gamma = 1.07$). These interpretations are consistent with the experimental observations in Fig. 10.

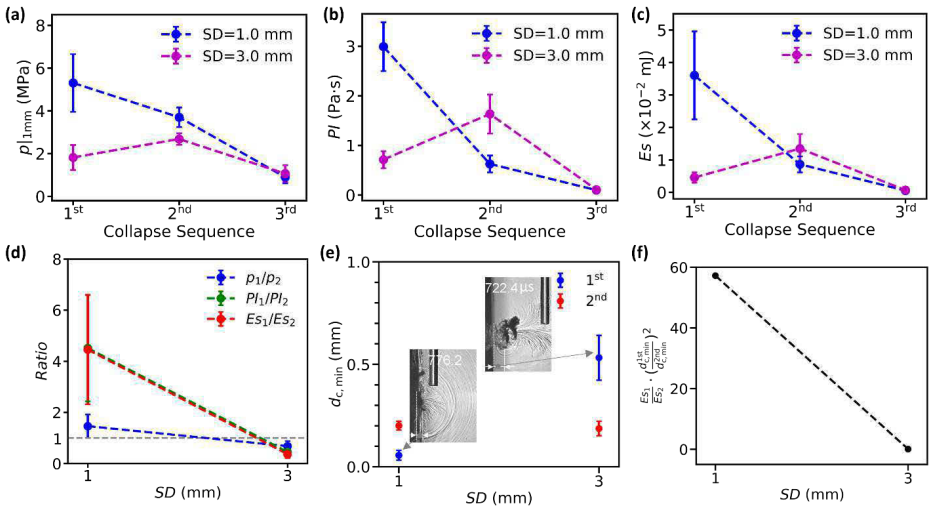

FIG. 12. Variations of (a) the maximum peak pressure, (b) pressure impulse (*PI*) and (c) acoustic energy associated with the shock wave emission (E_s) from the primary, secondary and tertiary collapse of LL-induced bubbles at different *SD*s. All the pressures are rescaled to values estimated at 1 mm distance from the bubble collapse site. (d) Ratios of p_1/p_2, PI_1/PI_2, and $E_{s,1}/E_{s,2}$ between the primary and secondary collapse of the bubble vs. *SD*. The subscripts "1" and "2" denote the primary and secondary collapse of the bubble, respectively. (e) Variations of the minimum distance ($d_{c,min}$) of the primary and secondary bubble collapsing spot from the solid boundary vs. *SD*. The insets are side-view images from the primary collapse of the bubbles. (f) Ratios of the acoustic energy density ($\frac{E_{S,1}}{E_{S,2}} \cdot \left(\frac{d^{2nd}_{c,min}}{d^{1st}_{c,min}}\right)^2$) delivered to the solid boundary between the primary and secondary collapse of the bubble vs. *SD*.

Fourth, the observation of Schmid head wave (SchW) when the toroidal bubble collapses in close proximity to the solid boundary (see 722.8 µs in Fig. 4(b) and 780 µs in Fig. 6(a)) clearly indicates the generation of *LRW* that is known to cause micro-fractures on the surface of brittle materials [41, 46, 47].

The role of *LRW* and other bulk and surface acoustic waves (generated by the bubble collapse during LL) in stone damage needs to be investigated thoroughly in the future, including compression-induced tensile fracture [48, 49] and interactions of tensile and shear waves with *LRW* away from the shock wave impact site [50]. In contrast to the deep drilling produced by photothermal ablation of the Ho:YAG laser when the fiber is aligned perpendicular to the stone surface, the superficial and dispersive damage created by the bubble collapse is more desirable for generating fine fragments from a thin layer on the stone surface during clinical dusting treatment [2, 7, 51, 52].

Moreover, the accurate detection of the time and location of various bubble collapsing events during LL by 3D-PCM (Fig. 9) and the close correlation of such acoustic mapping with the analogous damage patterns produced on the BegoStone surface (Fig. 10) demonstrate the great potential of 3D-PCM in cavitation detection in opaque materials [31] when the direct optical imaging is not available. Efforts are underway to use the 3D-PCM to track the variation of bubble dynamics as a proxy to non-invasively monitor the progression of stone damage during LL. Such a possibility is illustrated by the results in Figs. 2, 9 and 10.

Finally, the accumulation of crater damage on the stone surface (see Fig. 2) may modulate the dynamics of bubble collapse and damage progression [53-55] during LL. Future development of more advanced numerical models of multiphase flow-structure interaction [33, 34] relevant to LL is warranted to better appreciate the critical physical processes in bubble nucleation, growth, asymmetric collapse, shockwave emission, in relation to the pertinent thermal and mechanical mechanisms of stone damage that may help to improve the treatment efficiency while ensuring the safety of this popular surgery procedure for kidney stone patients.

V. CONCLUSIONS

In conclusion, we have investigated the effects of *SD* on the collapse of a "pear-shaped" vapor bubble induced by a Ho: YAG fiber laser near a parallel solid boundary. Our observations of the asymmetric collapse of the bubble with the development of multiple jets signify the boundary effect from the solid surface, the laser fiber, and the varying curvature along the bubble surface. At SD = 3.0 mm ($\gamma = 1.07$), the transverse jet penetrates the distal bubble wall during the primary collapse, producing an inverted "triangle-shaped" toroidal bubble translating toward the solid boundary. Shock wave emissions are generated by the self-intensified collapse of the toroidal bubble at multiple spots distant from the surface, and thus contribute minimally to the stone damage. Following a strong rebound, the toroidal bubble collapses again, much closer to the solid boundary and away from the fiber tip, with boosted secondary shock wave emissions of greater damage potential, which match well with the location of the damage patterns observed on the BegoStone surfaces. In comparison, at SD = 1.0 mm ($\gamma = 0.36$), the transverse jet, piercing through the bubble interior, impacts upon the solid boundary, generating a "horseshoe-shaped" toroidal bubble during the final stage of the primary collapse of the bubble. The collapse of the toroidal bubble is non-uniform and disrupted by the fiber and asymmetric radial flow following the jet impact. The strongest collapse occurs at two corners of the "horseshoe-shaped" toroidal bubble, boosted by the self-intensified collapsing process toward the end of each branch with the greatest damage potential confirmed by the "smiling-face" damage pattern. The subsequent rebound of the toroidal bubble is weak, and so is the ensuring secondary collapse with minimal contribution to the stone damage.

Most importantly, simultaneous high-speed imaging and 3D-PCM allow us to resolve the intricite details in the asymmetric collapse of LL-generated bubble with jet formation, and the non-uniform and self-intensified collapse of the toroidal bubble, and further correlate these unique cavitation features with the distinctly contrasting damage patterns produced on the stone surface at different SDs. The physical insights obtained from the present study are valuable for better understanding the mechanism of stone damage and for improving the treatment efficiency of LL [56]. The results may also benefit other fields related to cavitation, such as erosion mitigation in marine propellers and pipelines [43, 53].

Accepted to Phys. Fluids 10.1063/5.0139741

ACKNOWLEDGEMENTS

The authors would like to express their gratitude to Dornier MedTech for providing the H Solvo laser used in this study. This project is supported by the National Institute of Health (NIH) through grants 5P20 DK123970-02 and 2R01DK052985-24A1. X.Z. and K.W. also acknowledges the support of the National Science Foundation (NSF) under Award CBET-1751487.

SUPPLEMENTARY MATERIAL

See the supplementary material for the searching strategy of bubble collapsing locations and times in 3D-PCM, the (*x*, *y*, *z)* coordinates of the bubble-collapsing spots in Fig. 9.

REFERENCES

1. Ho, D.S., et al., *The role of cavitation in energy delivery and stone damage during laser lithotripsy.* Journal of Endourology, 2021. **35**(6): p. 860-870.
2. Chen, J., et al., *Cavitation Plays a Vital Role in Stone Dusting during Short Pulse Holmium: YAG Laser Lithotripsy.* Journal of endourology, 2021. **36**(5): p. 674-683.
3. Chen, J., et al., *The Effects of Scanning Speed and Standoff Distance of the Fiber on Dusting Efficiency during Short Pulse Holmium: YAG Laser Lithotripsy.* Journal of clinical medicine, 2022. **11**(17): p. 5048.
4. Fried, N.M., *Recent advances in infrared laser lithotripsy.* Biomedical Optics Express, 2018. **9**(9): p. 4552-4568.
5. Fried, N.M. and P.B. Irby, *Advances in laser technology and fibre-optic delivery systems in lithotripsy.* Nature Reviews Urology, 2018. **15**(9): p. 563-573.
6. Chan, K.F., et al., *A perspective on laser lithotripsy: The fragmentation processes.* Journal of Endourology, 2001. **15**(3): p. 257-273.
7. Chan, K.F., et al., *Holmium : YAG laser lithotripsy: A dominant photothermal ablative mechanism with chemical decomposition of urinary calculi.* Lasers in Surgery and Medicine, 1999. **25**(1): p. 22-37.
8. Keller, E.X., et al., *Fragments and dust after Holmium laser lithotripsy with or without "Moses technology": How are they different?* Journal of Biophotonics, 2019. **12**(4).
9. Teichman, J.M.H., et al., *Holmium : YAG lithotripsy: Photothermal mechanism converts uric acid calculi to cyanide.* Journal of Urology, 1998. **160**(2): p. 320-324.
10. Lauterborn, W. and H. Bolle, *Experimental Investigations of Cavitation-Bubble Collapse in Neighborhood of a Solid Boundary.* Journal of Fluid Mechanics, 1975. **72**(2): p. 391-399.
11. Lindau, O. and W. Lauterborn, *Cinematographic observation of the collapse and rebound of a laser-produced cavitation bubble near a wall.* Journal of Fluid Mechanics, 2003. **479**: p. 327-348.

12. Philipp, A. and W. Lauterborn, *Cavitation erosion by single laser-produced bubbles.* Journal of Fluid Mechanics, 1998. **361**: p. 75-116.
13. Vogel, A. and W. Lauterborn, *Acoustic Transient Generation by Laser-Produced Cavitation Bubbles near Solid Boundaries.* Journal of the Acoustical Society of America, 1988. **84**(2): p. 719-731.
14. Vogel, A., W. Lauterborn, and R. Timm, *Optical and Acoustic Investigations of the Dynamics of Laser-Produced Cavitation Bubbles near a Solid Boundary.* Journal of Fluid Mechanics, 1989. **206**: p. 299-338.
15. Tomita, Y. and A. Shima, *Mechanisms of Impulsive Pressure Generation and Damage Pit Formation by Bubble Collapse.* Journal of Fluid Mechanics, 1986. **169**: p. 535-564.
16. Gonzalez-Avila, S.R., F. Denner, and C.D. Ohl, *The acoustic pressure generated by the cavitation bubble expansion and collapse near a rigid wall.* Physics of Fluids, 2021. **33**(3).
17. Bussmann, A., et al., *Investigation of cavitation bubble dynamics near a solid wall by high-resolution numerical simulation.* Physics of Fluids, 2023.
18. Lechner, C., et al., *Fast, thin jets from bubbles expanding and collapsing in extreme vicinity to a solid boundary: A numerical study.* Physical Review Fluids, 2019. **4**(2): p. 021601.
19. Reuter, F., C. Deiter, and C.-D. Ohl, *Cavitation Erosion by Shockwave Self-Focusing of a Single Bubble.* Ultrasonics Sonochemistry, 2022: p. 106131.
20. Reuter, F. and C.-D. Ohl, *Supersonic needle-jet generation with single cavitation bubbles.* Applied Physics Letters, 2021. **118**(13): p. 134103.
21. Zhai, Y., et al., *Experimental study on the characteristics of microjets and shock waves of cavitation bubbles near elastic boundaries.* Ocean Engineering, 2022. **257**: p. 111664.
22. Dular, M., et al., *High speed observation of damage created by a collapse of a single cavitation bubble.* Wear, 2019. **418**: p. 13-23.
23. Asshauer, T., K. Rink, and G. Delacretaz, *Acoustic Transient Generation by Holmium-Laser-Induced Cavitation Bubbles.* Journal of Applied Physics, 1994. **76**(9): p. 5007-5013.

24. Frenz, M., et al., *Starting mechanisms and dynamics of bubble formation induced by a Ho: Yttrium aluminum garnet laser in water.* Journal of Applied Physics, 1998. **84**(11): p. 5905-5912.

25. Zhong, P., et al., *Transient cavitation and acoustic emission produced by different laser lithotripters.* J Endourol, 1998. **12**(4): p. 371-8.

26. Mohammadzadeh, M., et al., *Synthetic jet generation by high-frequency cavitation.* Journal of Fluid Mechanics, 2017. **823**.

27. Zhong, P., C.J. Chuong, and G.M. Preminger, *Characterization of Fracture-Toughness of Renal Calculi Using a Microindentation Technique.* Journal of Materials Science Letters, 1993. **12**(18): p. 1460-1462.

28. Li, M., *Deep Photoacoustic Imaging and Acoustic Cavitation Mapping in Shockwave Lithotripsy*. 2022.

29. Li, M.C., et al., *Tri-modality cavitation mapping in shock wave lithotripsy.* Journal of the Acoustical Society of America, 2021. **149**(2): p. 1258-1270.

30. Gyongy, M. and C.C. Coussios, *Passive Spatial Mapping of Inertial Cavitation During HIFU Exposure.* Ieee Transactions on Biomedical Engineering, 2010. **57**(1): p. 48-56.

31. Li, M.C., et al., *Simultaneous Photoacoustic Imaging and Cavitation Mapping in Shockwave Lithotripsy.* Ieee Transactions on Medical Imaging, 2020. **39**(2): p. 468-477.

32. Bilaniuk, N. and G.S.K. Wong, *Speed of Sound in Pure Water as a Function of Temperature.* Journal of the Acoustical Society of America, 1993. **93**(3): p. 1609-1612.

33. Cao, S., et al., *Shock-induced bubble collapse near solid materials: effect of acoustic impedance.* Journal of Fluid Mechanics, 2021. **907**.

34. Zhao, X., W. Ma, and K. Wang, *Simulating laser-fluid coupling and laser-induced cavitation using embedded boundary and level set methods.* Journal of Computational Physics, 2022: p. 111656.

35. Main, A., et al., *An enhanced FIVER method for multi-material flow problems with second-order convergence rate.* Journal of Computational Physics, 2017. **329**: p. 141-172.

36. Chew, L.W., et al., *Interaction of two differently sized oscillating bubbles in a free field.* Physical Review E, 2011. **84**(6).

37. Mishra, A., et al., *Flow focusing from interacting cavitation bubbles.* Physical Review Fluids, 2022. **7**(11): p. 110502.
38. Benjamin, T.B. and A.T. Ellis, *The collapse of cavitation bubbles and the pressures thereby produced against solid boundaries.* Philosophical Transactions for the Royal Society of London. Series A, Mathematical and Physical Sciences, 1966: p. 221-240.
39. Wang, Q.X., et al., *Numerical investigation of bubble dynamics at a corner.* Physics of Fluids, 2020. **32**(5).
40. Koukouvinis, P., et al., *Simulation of bubble expansion and collapse in the vicinity of a free surface.* Physics of Fluids, 2016. **28**(5).
41. Zhang, Y., et al., *Nanosecond shock wave-induced surface acoustic waves and dynamic fracture at fluid-solid boundaries.* Physical Review Research, 2019. **1**(3).
42. Trummler, T., S.J. Schmidt, and N.A. Adams, *Numerical investigation of non-condensable gas effect on vapor bubble collapse.* Physics of Fluids, 2021. **33**(9).
43. Brennen, C.E., *Cavitation and bubble dynamics*. 2014: Cambridge University Press.
44. Rayleigh, L., *VIII. On the pressure developed in a liquid during the collapse of a spherical cavity.* The London, Edinburgh, and Dublin Philosophical Magazine and Journal of Science, 1917. **34**(200): p. 94-98.
45. Sankin, G.N., et al., *Shock wave interaction with laser-generated single bubbles.* Physical Review Letters, 2005. **95**(3).
46. Abrate, S., B. Castanié, and Y.D. Rajapakse, *Dynamic failure of composite and sandwich structures*. Vol. 192. 2012: Springer Science & Business Media.
47. Xiang, G.M., et al., *Variations of stress field and stone fracture produced at different lateral locations in a shockwave lithotripter field.* Journal of the Acoustical Society of America, 2021. **150**(2): p. 1013-1029.
48. Lokhandwalla, M. and B. Sturtevant, *Fracture mechanics model of stone comminution in ESWL and implications for tissue damage.* Physics in Medicine and Biology, 2000. **45**(7): p. 1923-1940.

49. Huang, J.Y., et al., *Origin of compression-induced failure in brittle solids under shock loading.* Physical Review B, 2015. **92**(14).

50. Yang, C., *Mechanisms of Stone Fragmentation Produced by Nano Pulse Lithotripsy (NPL)*. 2017, Duke University.

51. Matlaga, B.R., et al., *Ureteroscopic Laser Lithotripsy: A Review of Dusting vs Fragmentation with Extraction.* Journal of Endourology, 2018. **32**(1): p. 1-6.

52. Humphreys, M.R., et al., *Dusting versus Basketing during Ureteroscopy-Which Technique is More Efficacious? A Prospective Multicenter Trial from the EDGE Research Consortium.* Journal of Urology, 2018. **199**(5): p. 1272-1276.

53. Gonzalez-Avila, S.R., et al., *Mitigating cavitation erosion using biomimetic gas-entrapping microtextured surfaces (GEMS).* Science Advances, 2020. **6**(13).

54. Trummler, T., et al., *Near-surface dynamics of a gas bubble collapsing above a crevice.* Journal of Fluid Mechanics, 2020. **899**.

55. Sun, Y., et al., *Cavitation bubble collapse in a vicinity of a rigid wall with a gas entrapping hole.* Physics of Fluids, 2022. **34**(7): p. 073314.

56. De Coninck, V., et al., *Ho:YAG laser lithotripsy in non-contact mode: optimization of fiber to stone working distance to improve ablation efficiency.* World Journal of Urology, 2019. **37**(9): p. 1933-1939.